Applied Nanoscience (2021) 11:849–860
https://doi.org/10.1007/s13204-020-01642-1

ORIGINAL ARTICLE

A facile, two-step synthesis and characterization of Fe_3O_4–$L_{Cysteine}$–graphene quantum dots as a multifunctional nanocomposite

Amirhossein Alaghmandfard[1] · **Hamid Reza Madaah Hosseini**[1]

Received: 27 September 2020 / Accepted: 27 November 2020 / Published online: 3 January 2021

Abstract
In this research, a facile, two-step synthesis of Fe_3O_4–$L_{Cysteine}$–graphene quantum dots (GQDs) nanocomposite is reported. This synthesis method comprises the preparation of GQDs via hydrothermal route, which should be conjugated to the $L_{Cysteine}$ functionalized core–shell magnetic structure with the core of about 7.5-nm iron oxide nanoparticle and 3.5-nm $L_{Cysteine}$ shell. $L_{Cysteine,}$ as a biocompatible natural amino acid, was used to link magnetite nanoparticles (MNPs) with GQDs. X-ray powder diffraction, Fourier-transform infrared spectroscopy, X-ray photoelectron spectroscopy, energy dispersive X-ray were used to investigate the presence and formation of MNPs, $L_{Cysteine}$ functionalized MNPs, and final hybrid nanostructure. Morphology and size distribution of nanoparticles were demonstrated by scanning electron microscopy and transmission electron microscopy. Finally, the magnetic and optical properties of the prepared nanocomposite were measured by vibrating sample magnetometer, ultraviolet–visible, and photoluminescence spectroscopy. The results show that Fe_3O_4–$L_{Cysteine}$–GQDs nanocomposite exhibits a superparamagnetic behavior at room temperature with high saturation magnetization and low magnetic coercivity, which are 28.99 emu/g and 0.09 Oe, respectively. This nanocomposite also shows strong and stable emission at 460 nm and 530 nm when it is excited with the 235 nm wavelength. The magnetic GQDs structure also reveals the absorption wavelength at 270 nm. Therefore, Fe_3O_4–$L_{Cysteine}$–GQDs nanocomposite can be considered as a potential multifunctional hybrid structure with magnetic and optical properties simultaneously. This nanocomposite can be used for a wide range of biomedical applications like magnetic resonance imaging (MRI) contrast agents, biosensors, photothermal therapy, and hyperthermia.

Keywords Magnetite nanoparticles · Graphene quantum dots · $L_{cysteine}$ · Magnetic characteristics · Optical properties

Introduction

During the past decade, the use of nanotechnology has become more prevalent among the various biomedical applications, specially bioimaging, drug delivery, antibacterial activities, and this is due to the high surface to volume ratio and remarkable chemical reaction of nanomaterials (Ghosal and Sarkar 2018; Hai 2018a, b; Nakhjavani 2017; Rajeshkumar and Naik 2018). Several nanomaterials, notably magnetite nanoparticles (MNPs), with their great properties, such as high magnetism, low toxicity, and having a remarkable biocompatible surface, have attracted enormous worldwide researchers' attention (Gao 2016; Powell 2020). Magnetic nanomaterials, e.g., superparamagnetic iron oxide nanoparticles (SPIONs), are prime candidates for a wide range of applications in biomedical sciences and technologies such as magnetite resonance imaging (MRI) contrast agent, cancer therapy, drug delivery, cell labeling, and tracking (Yang 2018; Huang 2016; Ahmadi and Gu 2012). According to the size and shape distribution of the MNPs, tremendous methods of synthesis have been developed, which the co-precipitation approach is one of the most convenient synthesis methods for biomedical applications (Dubey and Kain 2018; Kulkarni 2014). Besides, nanofluids' novel characteristics can be used in a wide range of applications, especially heat transfer, electronics, biomedicine, and food (Sarfaraz 2018, 2019a; b). Besides, nanofluids exhibit enhanced thermal

✉ Hamid Reza Madaah Hosseini
madaah@sharif.edu

[1] Department of Materials Science and Engineering, Sharif University of Technology, Azadi Avenue, P.O. Box 11155-9466, Tehran, Iran

conductivity and convective heat transfer as compared with other kinds of fluids (Shahsavar 2019; Akbari 2016; Bahmani 2018; Nazari 2020). Among all nanofluids, ferrofluids containing MNPs exhibit high nanoparticle stability with biomedical applications.

Particle aggregation due to the long-range Vander Waal's forces and their high inclination to oxidize are the bare MNPs' properties' unwilling characteristics. One of the most conventional and economic approaches to prevent these spontaneous features and improve the dispersion behavior in solutions of pristine MNPs is a surface modification (Farjadian 2016; Liu 2017). Amino acids are desirable agents among the surfactants as the fine ligands for nano-sized magnetite particle coating (Xia 2016). $L_{Cysteine}$ (L_{Cys}) is a biocompatible, natural amino acid with the formula of [$HO_2CCH(NH_2)CH_2SH$]. This amino acid has three functional groups, including carboxylic (-COOH), amino (-NH_2), and thiol (-SH). Therefore, $L_{Cysteine}$ with desirable binding properties could prevent the oxidation of MNPs and convert them to particles with significant solubility and stability in organic solutions and provides better bio-compatibility behavior for the final products (Bagbi 2017; Ahmadi 2011).

Recently, graphene, a two-dimensional (2D) carbon allotropy, has drawn considerable attention because of its superiority in novel electrical and optical properties compared to other materials. Graphene is the one-atom-thick sheet of sp^2 hybridized carbon atoms, which is arranged in a honeycomb-packed structure (Fang et al. 2015; Naumis 2016). Many researchers have studied graphene quantum dots (GQDs) as a zero-dimensional (0D) carbon material with a size of less than 100 nm in all dimensions. Owing to the edge effect and quantum confinement effect (QCE), GQDs possess novel and unique properties, which can never be seen in pristine materials (Hai 2018a, b; Zhang et al. 2018; Bacon 2014; Kim 2012). In comparison with some semiconductors, GQDs exhibit outstanding properties, such as high photostability against photoblinking and photobleaching, low toxicity, eco-friendly, and biocompatibility. GQDs have shown excellent performance in different areas of biological applications, especially in biosensing for detection of various moieties like inorganic ions, small organic molecules, and bio-macromolecules, as well as bioimaging for monitoring organs, tissues, and living cell, such as cell imaging, targeted imaging, diagnostic imaging, and in vivo imaging (Zhang and Ding 2018; Zheng 2015; Russo 2016; Hai et al. 2018a, b). The properties of the GQDs are directly correlated to their physical features, such as its size, shape, and edge configuration, which are affected by their synthesis methods (Gu 2016; Wang 2015).

Herein, this work reports a facile and novel method for synthesizing Fe_3O_4–$L_{Cysteine}$–GQDs multifunctional nanocomposite through two steps. While several research papers have been used different methods to obtain Fe_3O_4-GQDs nanostructure, we report a facile, two-step route to synthesize magnetic GQDs nanostructure. We also utilize $L_{Cysteine}$ to prevent MNPs from oxidation and activate its surface due to its functional groups, which act as a linker between magnetite nanoparticles and GQDs. However, several research works have been done on the individual elements that we used in the synthesized nanostructure, we produce the multifunctional hybrid nanocomposite with high magnetic property and stable optical characteristics that can be used in a wide range of biomedical application, especially MRI contrast agents and bioimaging.

Materials and methods

Chemical reagents

All chemical reactants and reagents used in this research were of analytical grade and were used as received without further purification. Iron (II) chloride tetrahydrate ($FeCl_2.4H_2O$, Merck, CAS number: 13478-10-9, Iron (III) chloride hexahydrate, ($FeCl_3.6H_2O$, Merck, CAS number:10025-77-1), ammonia solution 25% (NH_4OH, Merck, CAS number: 7664-41-7), Hydrochloric acid (HCl, Merck, CAS number: 7647-01-0), citric acid ($C_6H_8O_7$, Merck, CAS number: 77-92-9), sodium hydroxide (NaOH, Merck, CAS number: 1310–73-2), and $L_{Cysteine}$ ($C_3H_7NO_2S$, BioChem, CAS number: 52–90-4) were used as the synthesizing reagents.

Synthesis of $L_{Cysteine}$ functionalized MNPs

$L_{Cysteine}$ functionalized Fe_3O_4 nanoparticles were synthesized using the co-precipitation method. The process describes as follows: first, the MNPs were obtained by solving 4 mmol of $FeCl_3{\cdot}6H_2O$ and 2 mmol of $FeCl_2.4H_2O$ (molar ration 2:1), in 20 and 5 mL of the 2 M HCl, respectively. The obtained solutions were mixed and stirred in 40 °C for 15 min under N_2 atmosphere. As to obtain suitable pH in the range of 11–12 (Ahmadi 2011), 35 mL of NH_4OH 25% solution was dropwise added to the solution with the rate of 15 $^{drops}/_{min}$ to increase the pH of the solution. The black precipitates were collected from the water by magnetic decantation then washed 3 times with distilled water and acetone to remove impurities. The general reaction can be written as

$$Fe^{2+} + 2Fe^{3+} + 8OH^- \rightarrow Fe_3O_4 + 4H_2O. \quad (1)$$

Afterward, 0.370 gr MNPs with 10 mL water ultrasound for about 30 min. Immediately, 1 mmol $L_{Cysteine}$ (0.121 gr), dissolved in 5 mL distilled water for 10 min by ultrasonication the mixture at 25 °C, was dropwise added to the MNPs solution. Subsequently, the products were stirred overnight.

The synthesized nanoparticles should be dried at 50 °C at the oven for 24 h (Fig. 1a).

Synthesis of GQDs

Pristine GQDs was fabricated by pyrolyzing citric acid. In a typical run of GQDs preparation, 2 gr acid citric was put in the 5 mL beaker and heated for 30 min at 200 °C to turn the colorless citric acid powder to the pale orange liquid. Obtaining this temperature is essential in this process, because producing GQDs is not feasible at temperatures below 200 °C. The obtained liquid was mixed with the 100 mL of 0.25 M NaOH, and the solution was continuously stirring for about 5 min. Finally, the resultant solution was neutralized to pH = 7 by adding drops of 2 M HCl and cooling to room temperature. This solution should be stored in a dark place and temperature of about 15 °C (Fig. 1b).

Synthesis of core–shell structure of MNPs with GQDs

First, 0.268 gr of functionalized MNPs should be dispersed in 10 mL distilled water and stirred continuously for 15 min and subsequently, 15 mL GQDs were gradually added to the mixture and stirred for 24 h. After the one-day stirring of the solution, the resultant mixture was dried at 50 °C for 24 h. Synthesis of $L_{Cysteine}$ coated magnetic nanoparticles with GQDs leads to the formation of Fe_3O_4–$L_{Cysteine}$–GQDs nanocomposite as a dual-functional nanomaterial (Fig. 1c).

Analyses and characterizations

The X-ray diffraction patterns of powder samples were obtained by a PANalytical X'pert PRO MPD diffractometer using Cu-K_a radiation with a wavelength of 1.5406 Å. The Fourier-transform infrared (FT-IR) spectra were collected in transmission mode with a Thermo Nicolet AVATAR 360 FT-IR spectrometer in the spectral range of 400–4000 cm^{-1} at room temperature. FT-IR powder samples were dried at 50 °C before the fabrication of the KBr pellet. X-ray photoelectron (XPS) spectroscopy was carried out with a monochromatic Al K_a X-ray source using chamber pressures of about 10^{-8} Pa. Conventional transmission electron microscopy (TEM) observations were done using a Philips CM300 microscope to determine the average particle size and morphology of the powder on an accelerating voltage of 200 kV. The surface morphology of the sample was observed by the Tescan MIRA3 scanning electron (SEM) microscope. In addition, an MDK-VSM system was used for magnetic characterizations. The optical properties were evaluated using the Cary Eclipse photoluminescence (PL) spectrometer.

Results and discussion

X-ray powder diffraction (XRD) measurement

The XRD patterns of synthesized bare Fe_3O_4, Fe_3O_4–$L_{Cysteine}$, and Fe_3O_4–$L_{Cysteine}$–GQDs nanostructures in comparison with the standard pattern of Fe_3O_4 nanoparticles (JCPDS data, card no. 96-900-5815), and Fe_2O_3 nanoparticles (JCPDS data, card no. 96-101-1241) are presented in Fig. 2. According to the standard pattern of magnetite nanoparticles, which is shown in Fig. 2a, the well-match pattern can be observed in Fig. 2c and confirms the inverse spinel and face-centered cubic (FCC) structure of synthesized magnetite particles which is belonging to the Fe_3O_4 nanoparticles. The average crystalline size of the Fe_3O_4 nanoparticles was determined using the Debye–Scherrer formula and full-width at half-maximum (FWHM) of the three most intense peaks (Ahmadi and Hosseini 2013):

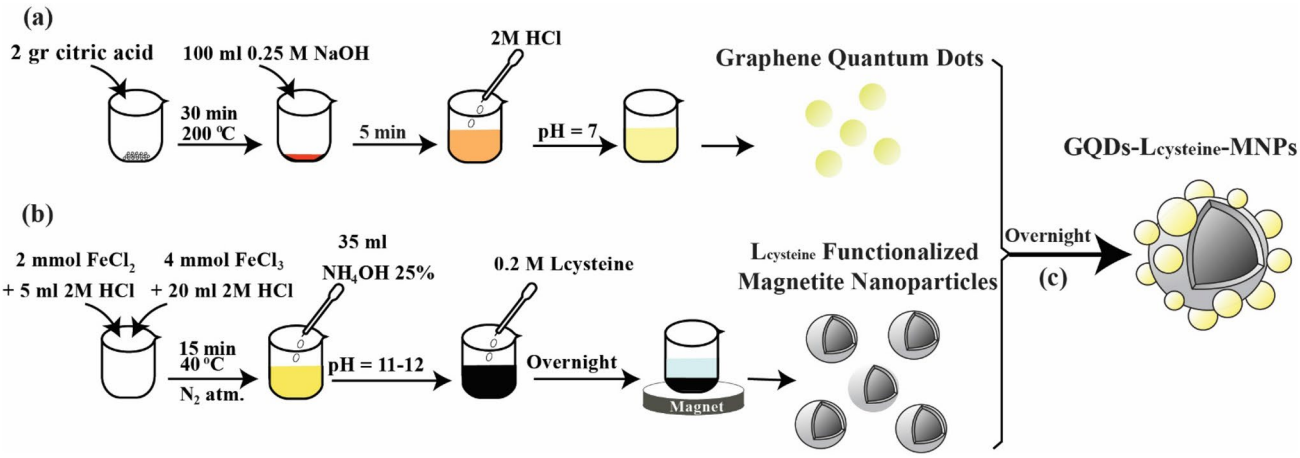

Fig. 1 Schematic representation of the synthesis approach of **a** GQDs by hydrothermal method and **b** $L_{cysteine}$ functionalized Fe_3O_4 nanoparticles by co-precipitation route to obtain **c** Fe_3O_4-$L_{cysteine}$-GQDs nanostructure

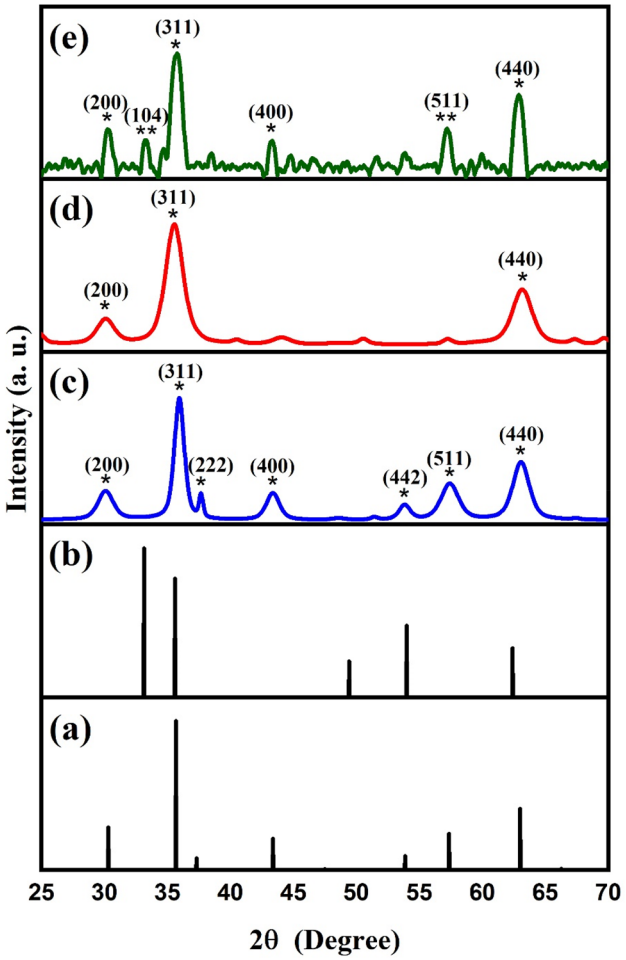

Fig. 2 Standard XRD pattern of the **a** pure Fe_3O_4 nanoparticles (JCPDS card no. 96-900-5815), **b** pure Fe_2O_3 nanoparticles (JCPDS card no. 96-101-1241), and XRD pattern of synthesized **c** naked, **d** $L_{cysteine}$–coated Fe_3O_4 nanoparticles, and **e** Fe_3O_4-$L_{cysteine}$-GQDs nanocomposites of the dried powder sample at room temperature

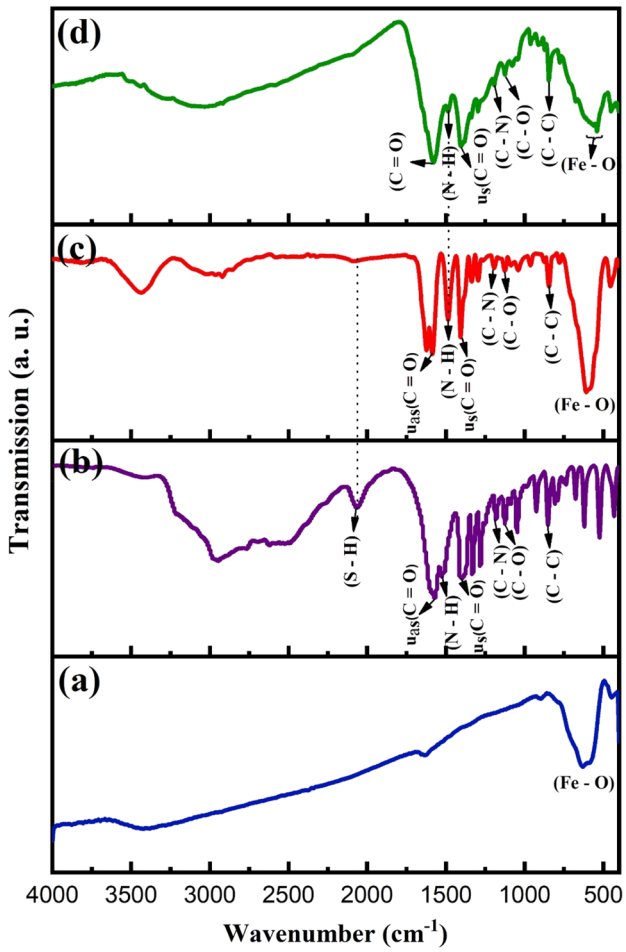

Fig. 3 Typical FT-IR spectra of the powder sample of **a** naked magnetite nanoparticles, **b** pure $L_{cysteine}$, **c** $L_{cysteine}$–coated Fe_3O_4 nanoparticles, and **d** Fe_3O_4-$L_{cysteine}$-GQDs nanocomposites at room temperature from 4000–400 cm^{-1}

$$D = \frac{0.9\lambda}{\beta \mathrm{Cos}(\theta)}, \tag{2}$$

where D is the mean crystalline size, l is the X-ray wavelength, b is the FWHM (radian) of diffraction peak, and θ is diffraction angle. According to the formula and diffraction patterns, the average crystal size of the Fe_3O_4 particles was calculated by about 7 nm. Figure 2d, e confirms that the presence of $L_{Cysteine}$ and GQDs did not considerably alter XRD patterns of the bare MNPs, so the nature and phase structure of the MNPs remains constant; however, it could be seen that some insignificant peaks with low intensity appear in the functionalized sample. The presence of GQDs can change some of the iron oxide nanoparticles' structure from Fe_3O_4 to Fe_2O_3. As a result, another peak at 33.35°, which is related to the (104) appears and confirms the formation of a Fe_2O_3.

Fourier-transform infrared (FT-IR) spectroscopy

The FT-IR spectra and characterization bands of Fe_3O_4–$L_{Cysteine}$–GQDs nanocomposites compare to the naked Fe_3O_4 nanoparticles' spectra, pure $L_{Cysteine}$, and Fe_3O_4–$L_{Cysteine}$ are shown in Fig. 3. Figure 3a shows the FT-IR spectra of uncoated Fe_3O_4 nanoparticles. The broad peak at 3423.40 cm^{-1} attributes to the presence of stretching and bending vibrations of the O–H bond and this is due to the entrapped moisture and adsorbed water. The two peaks at 572.82 cm^{-1} and 632.60 cm^{-1} are assigned to iron oxide nanoparticles' Fe–O bond vibration. The other peaks are related to the alkyl stretching modes, which were used during the synthesis procedure for pH rise. Figure 3b represents the $L_{Cysteine}$ FT-IR spectra. Typically, most of the amino

acids can exist as zwitterions, exhibiting both carboxylic (-COOH) and amino (-NH_2) functional groups (Sangeetha and Philip 2013). As mentioned above, $L_{Cysteine}$ is a neutral amino acid, so the FT-IR spectrum of the commercial $L_{Cysteine}$ shows broad characteristics range band of NH_3^+ stretching mode at 3000 cm^{-1}, and the N–H bond of the amino group is observed at 1501.05 cm^{-1}. The presence of the thiol group is virtually confirmed with the band at 2069.31 cm^{-1} (Hai et al. 2018a, b; Tiwari 2017). $L_{Cysteine}$ coated Fe_3O_4 nanoparticles show characteristic bands in FT-IR spectroscopy in Fig. 3c. These spectra exhibit insignificant changes in characteristic bonds compared with pristine $L_{Cysteine}$, shown in Table 1. The absence of the S–H band at 2069.31 cm^{-1} strongly shows that magnetite nanoparticles have been linked with the thiol group of $L_{Cysteine}$ to form a core–shell structure (Cohen 2008; Tiwari 2017; Karamipour 2015). The Fe–S peak cannot be seen in Fig. 3c, since Fe–S stretching, and bending peaks appear below 400 cm^{-1} (Lauterbach 2015). Finally, the FT-IR spectra of the final nanocomposite are depicted in Fig. 3d. A decrease in N–H characteristic band intensity can result in forming the bond between the amino acid functional group of $L_{Cysteine}$ and GQDs (Hasanzadeh 2016; Mohammad-rezaei 2014). The wide peak at 3000 cm^{-1} for the samples, including $L_{Cysteine}$ is related to the NH_3^+ stretching mode. The other characteristic bands with their wavenumber are shown in Table 1.

X-ray photoelectron spectroscopy (XPS) analysis

XPS measurement leads to a deeper understanding of the nature of the bonding types between $L_{Cysteine}$ and Fe_3O_4 nanoparticles. The results of the XPS analysis of $L_{Cysteine}$ functionalized Fe_3O_4 is shown in Fig. 4a, d. There are 5 distinct, sharp peaks at 710 eV, 531 eV, 401 eV, 288 eV, and 163 eV in the full spectrum, which are described as the Fe2p, O1s, N1s, C1s, and S2p, respectively (Fig. 4a). The possibility of forming the bonding of amino and carboxylic groups of $L_{Cysteine}$ to the Fe_3O_4 nanoparticles can be neglected, since the singlet spectrum of N1s and O1s in the $L_{Cysteine}$ functionalized Fe_3O_4 is detected, which are correlated to the amino and carboxylic groups of the $L_{Cysteine}$ molecules. In the C1s spectrum in Fig. 4b, three peaks, which are detected at 288.2 eV, 287.6 eV, and 285.1 eV, ascribe the presence of C–C, C–N/C–H/C–OH, and C = O, respectively and show the existence of $L_{Cysteine}$ in the final product. These spectra also announce that the carboxyl group in $L_{Cysteine}$ molecules did not react with the iron oxide nanoparticles. Therefore, according to the most similar research, the most probable binding type is the formation of the Fe–S bond (Ahmadi 2011; Sangeetha and Philip 2013; Cohen 2008). The S2p XPS spectra of MNPs functionalized with $L_{Cysteine}$ is observed in Fig. 4c. Instead of two peaks at 163.7 eV and 164.8 eV for pure $L_{Cysteine}$, other characteristic peaks appear at 161.2 eV and 162.8 eV, Which confirm the chemical bond of Fe–S in the core–shell structure and assure us that the $L_{Cysteine}$ interacts with Fe_3O_4 nanoparticles via its thiol group (Cohen 2008). The peaks at 709.5 eV and 722.9 eV reveal the Fe2p spectrum for the functionalized MNPs and associate to the MNPs chemical bonds (Fig. 4d). Besides, compared with the bare MNPs, a doublet peak is detected at 717.19 eV and 731.4 eV when the particles coated with $L_{Cysteine}$. The presence of 2 additional peaks at Fe2p XPS spectra of core–shell structure compare to the bare MNPs is due to the doublet nature of the excited ions, where the final state is available with two possible energies, formed from a set of degenerated states. These states of energies depend on the total angular momentum quantum number j = l + s, where l is the orbital angular momentum number and s is the spin angular momentum quantum number.

Scanning electron microscopy (SEM) characterization

SEM images of Fe_3O_4, Fe_3O_4–$L_{Cysteine}$, and Fe_3O_4–$L_{Cysteine}$–GQDs nanostructures, shown in Fig. 5a–c, illustrate the homogenized distribution and

Table 1 The list of characteristic band wavenumber of $L_{Cysteine}$, $L_{Cysteine}$ coated MNPs, and Fe_3O_4-$L_{Cysteine}$-GQDs

Sample	Bare MNPs (cm^{-1})	$L_{Cysteine}$ (cm^{-1})	$L_{Cysteine}$ coated MNPs (cm^{-1})	MNPs-$L_{Cysteine}$-GQDs (cm^{-1})
Band assignment				
Fe–O	572.82		576.64	510–600
	632.60		607.70	
υ_s(C=O)		1395.37	1406.25	1403.30
υ_{as}(C=O)		1576.97	1580.65	1577.85
N–H		1501.05	1485.07	1487.63
S–H		2069.31		
C–N		1189.32	1192.69	1195.99
C–O		1125.13	1126.01	1125.03
C–C		848.6	844.92	846.36

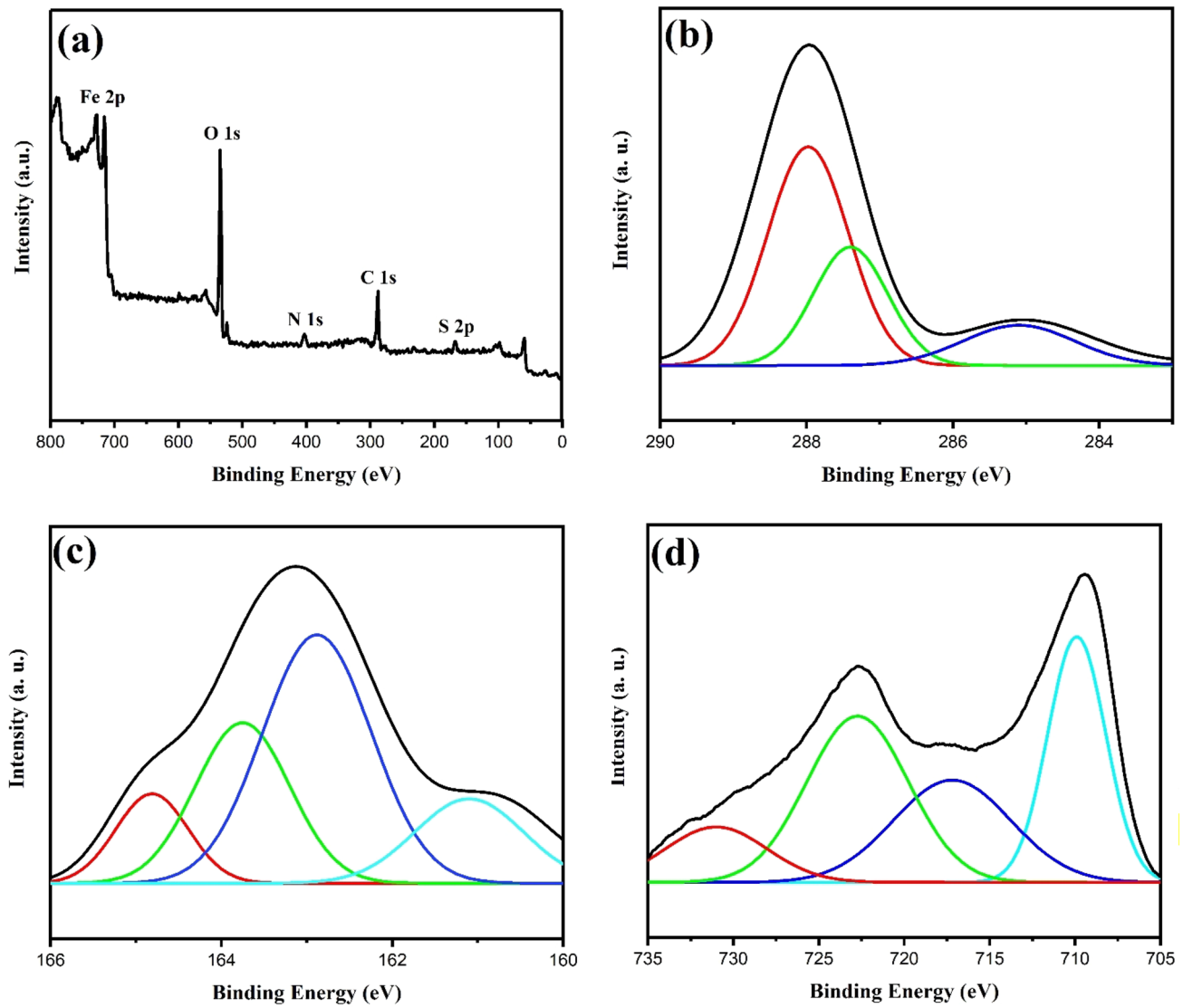

Fig. 4 XPS spectra of $L_{cysteine}$–coated Fe_3O_4 nanoparticles of **a** overview, and the high-resolution spectra of **b** C1s, **c** S2p, and **d** Fe2p with a monochromatic Al K_α X-ray source using chamber pressures of 10^{-8} Pa at room temperature

sponge-like morphology of all samples in which the mean size of the particles is about 15–20 nm. Although the excellent stability and high dispersion of nanoparticles of magnetite in an aqueous solution, they aggregate as soon as they dry. Therefore, in this micrograph, each cluster has a number of smaller particles of magnetic nanoparticles. Furthermore, EDX measurements were used to confirm the composition of the synthesized samples (Fig. 5d–f). The quantity of the Fe, O, C, N, and S contents are shown in Table 2. The calculated elements' content quantities reveal the successful deposition of the MNPs–$L_{Cysteine}$–GQDs nanocomposites.

Transmission electron microscopy (TEM) characterization

TEM images in Fig. 6a refer to the naked Fe_3O_4 in the absence of $L_{Cysteine,}$ and Fig. 6b is related to the modified Fe_3O_4 with $L_{Cysteine}$. As shown in Fig. 6a, bare iron oxide particles have a high tendency to aggregate due to their strong magnetic and long-range Vander Waal's forces. Figure 6b shows Fe_3O_4 particles functionalized with $L_{Cysteine}$ and its dispersion behavior. The core size of the particles has been increased during the functionalization process. It is clear from size distribution histogram diagrams in Fig. 6c, d, the

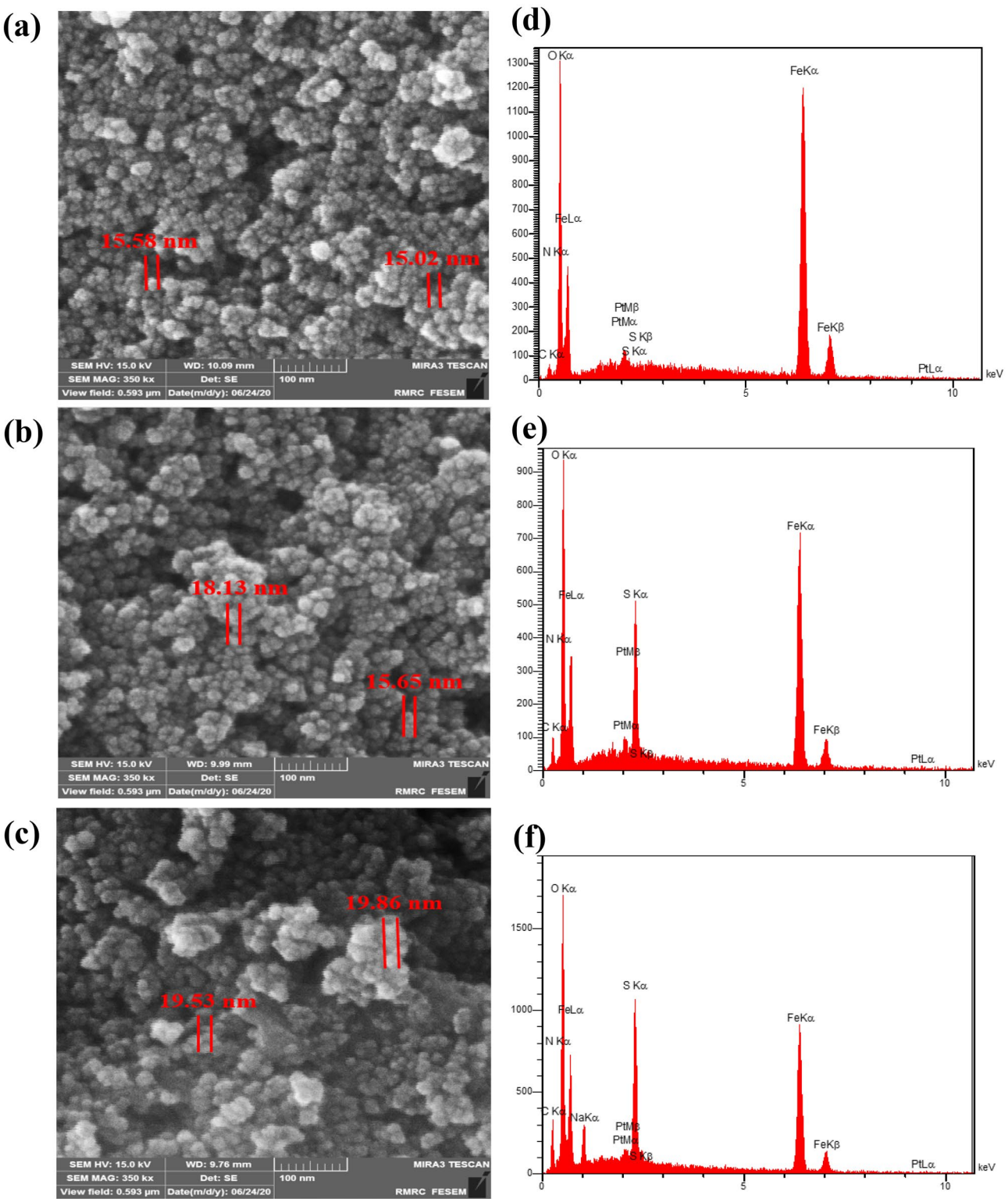

Fig. 5 FESEM micrograph of **a** naked, **b** $L_{cysteine}$-coated Fe_3O_4 nanoparticles, **c** Fe_3O_4-$L_{cysteine}$-GQDs nanocomposites of a dried sample which are coated with Pt and particle size range from 15 to 20 nm, and EDX spectra of **d** naked, **e** $L_{cysteine}$-coated Fe_3O_4 nanoparticles, **f** Fe_3O_4-$L_{cysteine}$-GQDs nanocomposites in a vacuum atmosphere

Table 2 Elements' content quantities of Fe_3O_4, $L_{cysteine}$–coated Fe_3O_4 nanoparticles and Fe_3O_4-$L_{Cysteine}$-GQDs nanocomposite measured by EDX spectra

Element	Fe (wt. %)	O (wt. %)	Fe/O	C (wt. %)	N (wt. %)	S (wt. %)	Pt (wt. %)
Sample							
Fe_3O_4	60.67	33.12	1.83	0	0	0	6.21
Fe_3O_4–$L_{cysteine}$	41.83	32.42	1.29	11.26	2.98	5.58	5.93
Fe_3O_4–$L_{cysteine}$–GQDs	27.70	36.32	0.76	17.86	6.42	6.14	5.56

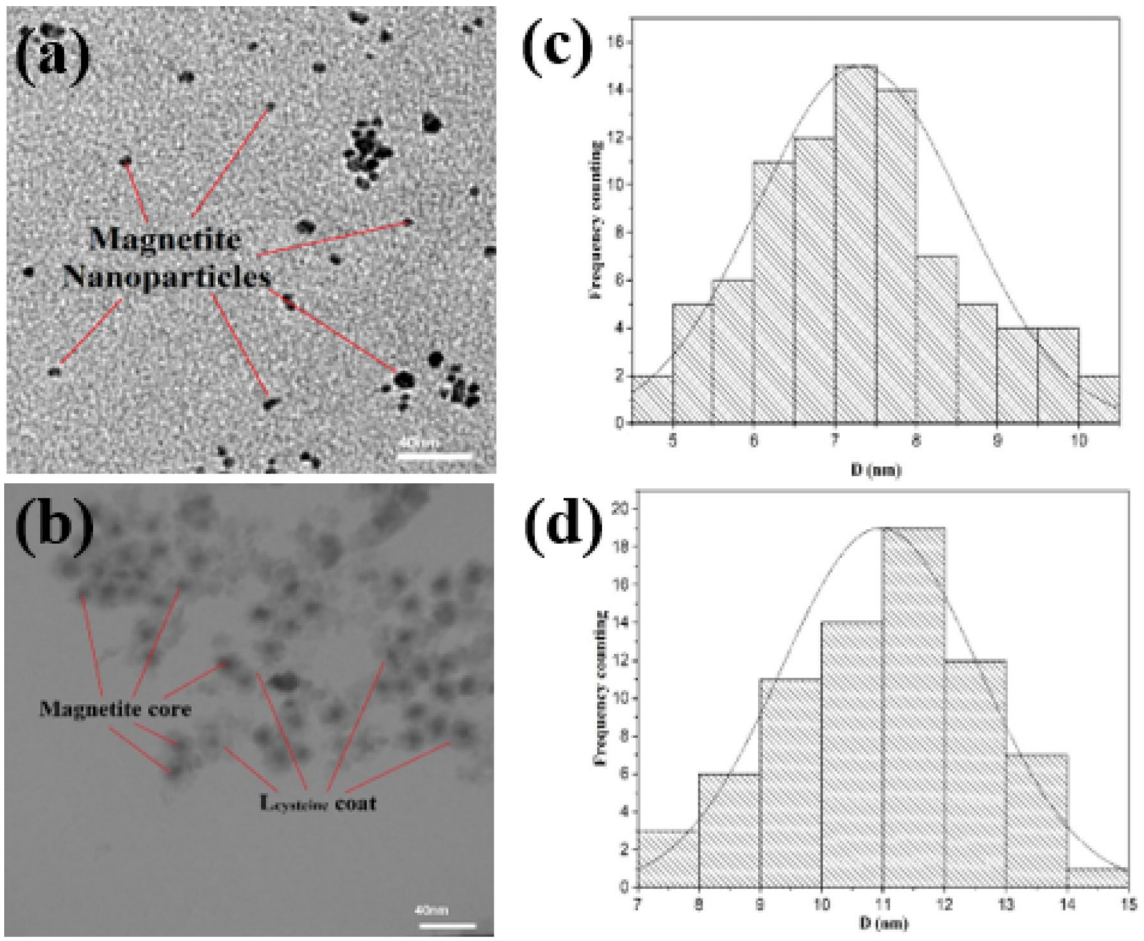

Fig. 6 TEM micrographs of **a** naked, **b** $L_{cysteine}$-coated Fe_3O_4 nanoparticles, and with their corresponding particle size distribution of **c** naked, **d** $L_{cysteine}$–coated Fe_3O_4 nanoparticles with 7.5 ± 3 nm, and 11 ± 4 nm, respectively

mean particle size for Fe_3O_4 nanoparticles, Fe_3O_4–$L_{Cysteine}$ core–shell structure, and $L_{Cysteine}$ layer thickness are about 7.5 ± 3 nm, 11 ± 4 nm, and 3 ± 1 nm, respectively.

Vibrating sample magnetometer (VSM) diagrams

Magnetic hysteresis curves of the as-prepared Fe_3O_4, Fe_3O_4–$L_{Cysteine}$, and Fe_3O_4–$L_{Cysteine}$–GQDs structures at room temperature are depicted in Fig. 7a–c. The values of saturation magnetization (M_s), remnant magnetization (M_r), and magnetic coercivity (H_c) for all of the prepared samples show a superparamagnetic behavior and reveal their small size (Table 3). As it can be observed from data in Table 3, the superparamagnetic behavior of the bare Fe_3O_4 nanoparticles is confirmed from the high M_s and low H_c, which are 56.5 emu. g^{-1} and 0.28 Oe, respectively. Additionally, M_s decreases to 53.3 emu. g^{-1} when $L_{Cysteine}$ is coated MNPs, while H_c merely increases and reaches to 0.38 Oe. In other words, due to the core–shell interface and shielding effects, the $L_{Cysteine}$ layer decreases the magnetic properties compared with the bare magnetite nanoparticles**.** Finally, magnetic saturation for the Fe_3O_4–$L_{Cysteine}$–GQDs nanocomposite decreases to 28.99 emu. g^{-1}, while the H_c reaches 0.09 Oe. Although the presence of GQDs decreases the M_s, the

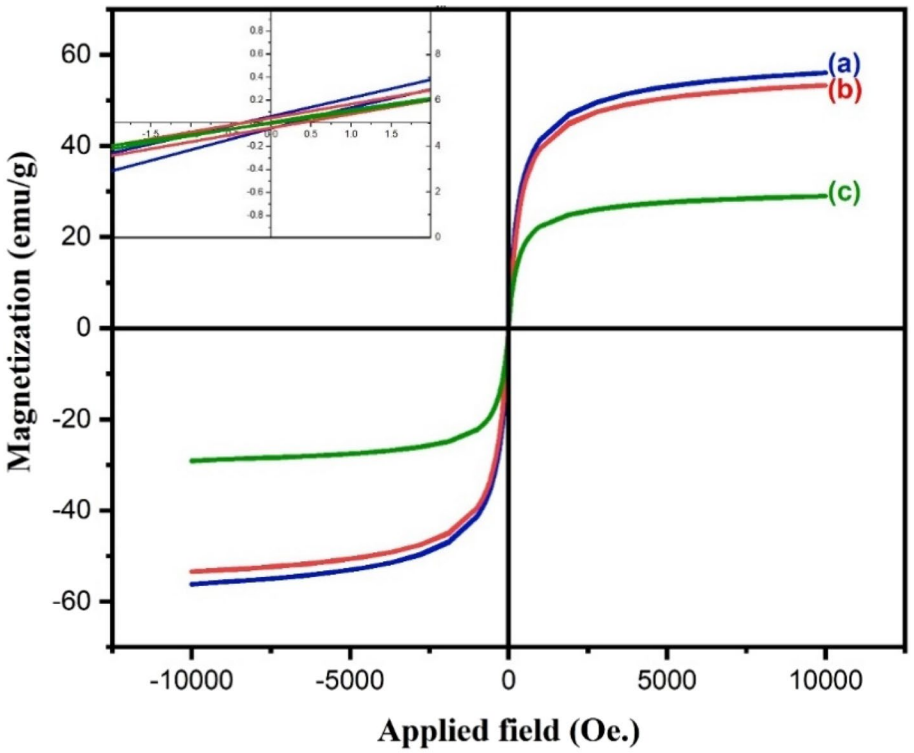

Fig. 7 Magnetic hysteresis curve of **a** bare Fe_3O_4 nanoparticle **b** $L_{cysteine}$ coated Fe_3O_4 and **c** Fe_3O_4-$L_{cysteine}$-GQDs nanocomposites at room temperature. These nanostructures exhibit superparamagnetic behavior with high M_s, and low H_c

Table 3 Magnetic properties of Fe_3O_4, $L_{cysteine}$-coated Fe_3O_4 nanoparticles and Fe_3O_4-$L_{Cysteine}$-GQDs nanocomposite

Magnetic parameter	M_s (emu/g)	H_c (Oe.)	M_r (emu/g)
Sample			
Fe_3O_4	56.88	0.28	0.69
Fe_3O_4–$L_{cysteine}$	53.79	0.38	0.04
Fe_3O_4–$L_{cysteine}$–GQDs	28.99	0.09	0.06

nanostructure still shows superparamagnetic properties. The reduction in M_s value has been referred to the disordering of the magnetic moment. The higher the GQDs shell thickness onto the magnetite nanoparticles leads to the lower magnetization saturation. Additionally, according to the XRD analysis, the change in the structure of Fe_3O_4–Fe_2O_3 is another reason to cause a decrease in the M_s value. As a result of the nanocomposite's magnetic–nonmagnetic hybridization, these results are still sufficient for MRI contrast agents.

Optical study

The UV–Vis spectra of GQDs and MNPs covered with GQDs lead to a strong absorption peak at 276 nm and 270 nm with a tail extending to the visible region, respectively (Fig. 8a, b). The high UV–Vis adsorption is due to the presence of the GQDs, which leads to the surface sphere and surface cavity mode at the interface of MNPs and GQDs. Photoluminescence (PL) spectra of the GQDs, MNPs, and Fe_3O_4–$L_{Cysteine}$–GQDs nanocomposites are recorded at room temperature (Fig. 8c–e). A detailed PL study for GQDs was carried out using different excitation wavelengths. Apart from most of the carbon-based nanomaterials with highly dependent PL excitation wavelength, GQDs show a different behavior (Mohammadrezaei 2014; Li 2010). As it can be seen in Fig. 8c, the emission wavelength of GQDs is nearly excitation-independent (Zhuo et al. 2012). By getting deeper in Fig. 8c, it can be observed that as the excitation wavelength varies from 235 to 400 nm, GQDs emit a stable, strong PL peak at about 460 nm (2.69 eV). This phenomenon happens when the size and sp^2 clusters on the surface of the GQDs remain constant and uniform (Dong 2012). Besides, the PL spectra of the bare MNPs revealed a stable emission at 530 nm (2.34 eV) when it is excited at 235 nm (Fig. 8d). The distinct PL features and different emission wavelengths in the visible range were measured with photoexcitation at 235 nm for the final product, which presents an asymmetric emission curve (Fig. 8d). Figure 8d shows a broad emission peak at around the visible range with two unequivocal adsorption peaks at about 460 nm and 530 nm. It is clear that the former peak nearly stands at the same position compare with the pristine GQDs, while the second peak can be ascribed to the presence of magnetic core in the final nanocomposites. As a result, the PL spectra of the final product shows a stable emission in the

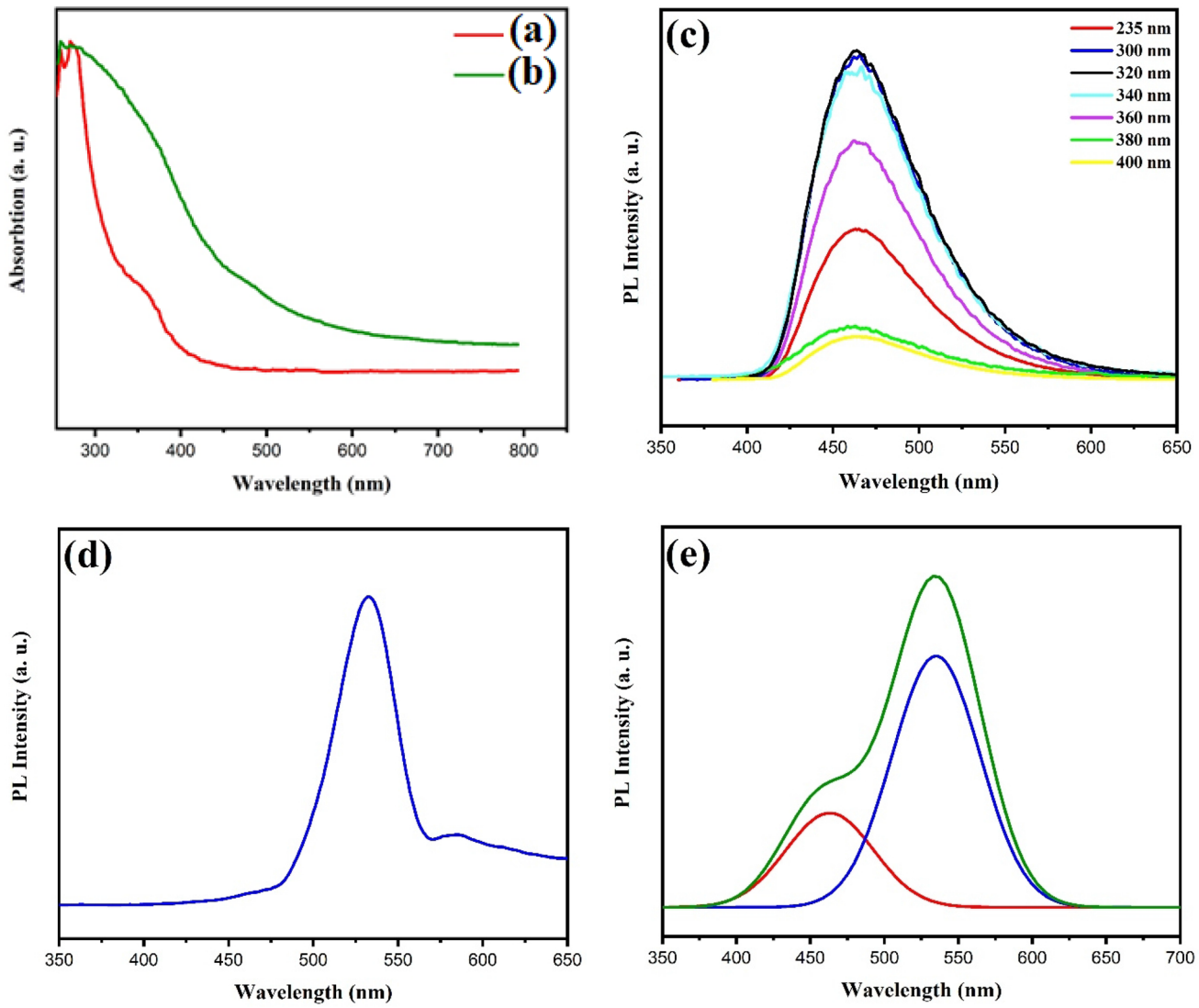

Fig. 8 The UV–Vis spectra of **a** as prepared GQDs, and **b** Fe_3O_4 -$L_{Cysteine}$-GQDs nanostructure from 250 to 800 nm and photoluminescence spectra of **c** GQDs at different excitation wavelength ranging from 235 to 400 nm reveals a stable emission at 465 nm, **d** magnetite nanoparticles at 235 nm excitation wavelength, which shows emission at 530 nm, and **e** Fe_3O_4-$L_{Cysteine}$-GQDs at room temperature at 235 nm excitation wavelength, which shows stable emission in the visible range at 460 nm and 530 nm

visible range, which makes this nanocomposite a promising candidate for bioimaging applications.

Conclusion

In this research, Magnetite nanoparticles were synthesized via a co-precipitation method and were coated with $L_{Cysteine}$ to produce a core–shell structure, while GQDs were obtained by hydrothermal approaches. Finally, a facile, two-step method was developed to synthesize Fe_3O_4–$L_{cysteine}$–GQDs nanocomposite. In this nanocomposite, $L_{Cysteine}$ acts as a linker between MNPs and GQDs and improves the MNPs' biocompatibility, and protects them from excessive oxidation and agglomeration. XRD analysis confirms the formation of the synthesized MNPs, $L_{Cysteine}$ coated MNPs, and MNPs–$L_{Cysteine}$–GQDs nanostructure. The XPS and FT-IR measurements reveal the formation of Fe–S bond between MNPs and $L_{Cysteine}$, so $L_{Cysteine}$ molecules bind to the MNPs via its thiol groups. SEM and TEM images show that MNPs have a high tendency to agglomerate and exhibit sponge-like morphologies with 7.5 ± 3 nm magnetic core. Additionally, EDX results show the weight percent of different elements in the samples. VSM diagram reveals superparamagnetic behavior with high M_s and negligible H_c for the final product. Investigation of optical properties from the UV–Vis and PL spectra confirm that the final nanocomposite reveals a desirable photoluminescence behavior in the visible range.

These results show that the obtained nanocomposite reveals proper magnetic characteristics and stable optical properties simultaneously. According to the conclusion mentioned above, the synthesized hybrid nanostructure reveals a suitable emission in the visible range and can be used in biosensors for detecting different cancer cells and viruses like breast cancers, COVID-19, and HIV. In addition, due to the final composite's superparamagnetic behavior, this nanostructure can also be used as an MRI contrast agent. In addition, increasing outcomes with magnetic nanostructures in recent in vivo research suggest the huge potential for cancer diagnostic and therapy. In recent years, treating and sensing molecules, cancer cells, and viruses are multi-billion-dollar industries among academia, clinicians, and biomedical engineers.

Acknowledgements The authors wish to thank the members of the Chemistry and Magnetic Materials laboratory at the Sharif University of Technology for their kind assistance and useful advice in the experimental section.

Compliance with ethical standards

Conflict of interest The authors declare no competing financial interest.

References

Ahmadi R, Gu N (2012) Characterization of cysteine coated magnetite nanoparticles as MRI contrast agent. Nano-Micro Lett 4(3):180–183. https://doi.org/10.1007/BF03353711

Ahmadi R, Hosseini H (2013) An investigation on the optimum conditions of synthesizing a magnetite based ferrofluid as MRI contrast agent using Taguchi method. Mater Sci Pol 31(2):253–258. https://doi.org/10.2478/s13536-012-0098-9

Ahmadi, et al (2011) Ultrasonic-assisted synthesis of magnetite based MRI contrast agent using cysteine as the biocapping coating. Mater Chem Phys 131(1–2):170–177. https://doi.org/10.1016/j.matchemphys.2011.04.083

Akbari OA, Safaei MR, Goodarzi M, Akbar NS, Zarringhalam M, Shabani GAS, Dahari M (2016) A modified two-phase mixture model of nanofluid flow and heat transfer in a 3-D curved microtube. Adv Powder Technol 27(5):2175–2185. https://doi.org/10.1016/j.apt.2016.08.002

Bacon M, Bradley SJ, Nann T (2014) Graphene quantum dots. Part Part Syst Charact 31(4):415–428. https://doi.org/10.1002/ppsc.201300252

Bagbi Y, Sarswat A, Mohan D, Pandey A, Solanki PR (2017) Lead and chromium adsorption from water using L-cysteine functionalized magnetite (Fe_3O_4) Nanoparticles. Sci Rep 7(1):1–15. https://doi.org/10.1038/s41598-017-03380-x

Bahmani MH, Sheikhzadeh G, Zarringhalam M, Akbari OA, Alrashed AA, Shabani GAS, Goodarzi M (2018) Investigation of turbulent heat transfer and nanofluid flow in a double pipe heat exchanger. Adv Powder Technol 29(2):273–282. https://doi.org/10.1016/j.apt.2017.11.013

Cohen H, Gedanken A, Zhong Z (2008) One-step synthesis and characterization of ultrastable and amorphous Fe_3O_4 colloids capped with cysteine molecules. J Phys Chem C 112:15429–15438

Dong Y, Shao J, Chen C, Li H, Wang R, Chi Y, Lin X, Chen G (2012) Blue luminescent graphene quantum dots and graphene oxide prepared by tuning the carbonization degree of citric acid. Carbon 50(12):4738–4743. https://doi.org/10.1016/j.carbon.2012.06.002

Dubey V, Kain V (2018) Synthesis of magnetite by coprecipitation and sintering and its characterization. Mater Manuf Processes 33(8):835–839. https://doi.org/10.1080/10426914.2017.1401720

Fang Q, Shen Y, Chen B (2015) Synthesis, decoration and properties of three-dimensional graphene-based macrostructures: a review. Chem Eng J 264:753–771. https://doi.org/10.1016/j.cej.2014.12.001

Farjadian F, Ghasemi S, Mohammadi-Samani S (2016) Hydroxyl-modified magnetite nanoparticles as novel carrier for delivery of methotrexate. Int J Pharmaceut 504(1–2):110–116. https://doi.org/10.1016/j.ijpharm.2016.03.022

Gao R, Cui X, Hao Y, Zhang L, Liu D, Tang Y (2016) A highly-efficient imprinted magnetic nanoparticle for selective separation and detection of 17 b -estradiol in milk. Food Chem 194:1040–1047. https://doi.org/10.1016/j.foodchem.2015.08.112

Ghosal K, Sarkar K (2018) Biomedical applications of graphene nanomaterials and beyond biomedical applications of graphene nanomaterials and beyond. ACS Biomater Sci Eng. https://doi.org/10.1021/acsbiomaterials.8b00376

Gu J, Zhang X, Pang A, Yang J (2016) Facile synthesis and photoluminescence characteristics of blue-emitting nitrogen-doped graphene quantum dots. Nanotechnology 27(16):165704. https://doi.org/10.1088/0957-4484/27/16/165704

Hai X, Feng J, Chen X, Wang J (2018a) Tuning the optical properties of graphene quantum dots for biosensing and bioimaging. J Mater Chem B 6(20):3219–3234. https://doi.org/10.1039/c8tb00428e

Hai X, Wang Y, Hao X, Chen X, Wang J (2018b) Folic acid encapsulated graphene quantum dots for ratiometric pH sensing and specific multicolor imaging in living cells. Sens Actuators B 268:61–69. https://doi.org/10.1016/j.snb.2018.04.090

Hasanzadeh M, Karimzadeh A, Shadjou N, Mokhtarzadeh A, Bageri L (2016) Graphene quantum dots decorated with magnetic nanoparticles : synthesis, electrodeposition, characterization and application as an electrochemical sensor towards determination of some amino acids at physiological pH. Mater Sci Eng, C 68:814–830. https://doi.org/10.1016/j.msec.2016.07.026

Huang J, Li Y, Orza A, Lu Q, Guo P, Wang L (2016) Magnetic nanoparticle facilitated drug delivery for cancer therapy with targeted and image-guided approaches. Adv Funct Mater. https://doi.org/10.1002/adfm.201504185

Karamipour S, Sadjadi MS, Farhadyar N (2015) Fabrication and spectroscopic studies of folic acid-conjugated Fe_3O_4@Au core-shell for targeted drug delivery application. Spectrochim Acta Part A 148:146–155. https://doi.org/10.1016/j.saa.2015.03.078

Kim S, Hwang SW, Kim MK, Shin DY, Shin DH, Kim CO, Yang SB, Park JH, Hwang E, Choi SH, Ko G (2012) Anomalous behaviors of visible luminescence from graphene quantum dots: interplay between size and shape. ACS Nano 6(9):8203–8208. https://doi.org/10.1021/nn302878r

Kulkarni SA, Sawadh PS, Palei PK, Kokate KK (2014) Effect of synthesis route on the structural, optical and magnetic properties of Fe_3O_4 nanoparticles. Ceram Int 40:1945–1949. https://doi.org/10.1016/j.ceramint.2013.07.103

Lauterbach L, Wang H, Horch M, Gee LB, Yoda Y, Tanaka Y, Zebger I, Lenz O, Cramer SP (2015) Nuclear resonance vibrational spectroscopy reveals the FeS cluster composition and active site vibrational properties of an O 2-tolerant NAD+-reducing [NiFe] hydrogenase. Chem Sci 6(2):1055–1060. https://doi.org/10.1039/C4SC02982H

Li H et al (2010) Water-soluble fluorescent carbon quantum dots and photocatalyst design. Angew Chem Int Ed 49(26):4430–4434

Liu Y, Yang J, Xie M, Xu J, Li Y, Shen H, Hao J (2017) Synthesis of polyethyleneimine-modified magnetic iron oxide nanoparticles without adding base and other additives. Mater Lett. https://doi.org/10.1016/j.matlet.2017.01.056

Mohammad-rezaei R, Razmi H, Abdollahi V, Matin AA (2014) Analytical Methods graphene quantum dots nanocomposite as an efficient adsorbent in magnetic solid phase extraction : application to determination of bisphenol A in water samples. Anal Methods 6:8413–8419. https://doi.org/10.1039/C4AY01633E

Nakhjavani M, Nikkhah V, Sarafraz MM, Shoja S, Sarafraz M (2017) Green synthesis of silver nanoparticles using green tea leaves: experimental study on the morphological, rheological and antibacterial behaviour. Heat Mass Transf 53(10):3201–3209. https://doi.org/10.1007/s00231-017-2065-9

Naumis GG, Barraza-Lopez S, Oliva-Leyva M, Terrones H (2016) A review of the electronic and optical properties of strained graphene and other similar 2D materials. Rep Prog Phys 80(9):96501. https://doi.org/10.1088/1361-6633/aa74ef

Nazari S, Ellahi R, Sarafraz MM, Safaei MR, Asgari A, Akbari OA (2020) Numerical study on mixed convection of a non-Newtonian nanofluid with porous media in a two lid-driven square cavity. J Therm Anal Calorim 140(3):1121–1145. https://doi.org/10.1007/s10973-019-08841-1

Powell CD, Atkinson AJ, Ma Y, Marcos-hernandez M, Villagran D, Westerhoff P, Wong MS (2020) Magnetic nanoparticle recovery device (MagNERD) enables application of iron oxide nanoparticles for water treatment. J Nanopart Res. https://doi.org/10.1007/s11051-020-4770-4

Rajeshkumar S, Naik P (2018) Synthesis and biomedical applications of cerium oxide nanoparticles–a review. Biotechnology Reports 17:1–5. https://doi.org/10.1016/j.btre.2017.11.008

Russo P, Liang R, Jabari E, Marzbanrad E, Toyserkani E, Zhou YN (2016) Single-step synthesis of graphene quantum dots by femtosecond laser ablation of graphene oxide dispersions. Nanoscale 8(16):8863–8877. https://doi.org/10.1039/c6nr01148a

Sangeetha J, Philip J (2013) Synthesis, characterization and antimicrobial property of Fe 3O4-Cys-HNQ nanocomplex, with l-cysteine molecule as a linker. RSC Advances 3(21):8047–8057. https://doi.org/10.1039/c3ra00005b

Sarafraz MM, Arya H, Saeedi M, Ahmadi D (2018) Flow boiling heat transfer to MgO-therminol 66 heat transfer fluid: experimental assessment and correlation development. Appl Therm Eng 138:552–562. https://doi.org/10.1016/j.applthermaleng.2018.04.075

Sarafraz MM, Yang B, Pourmehran O, Arjomandi M, Ghomashchi R (2019a) Fluid and heat transfer characteristics of aqueous graphene nanoplatelet (GNP) nanofluid in a microchannel. Int Commun Heat Mass Transfer 107:24–33. https://doi.org/10.1016/j.icheatmasstransfer.2019.05.004

Sarafraz MM, Safaei MR, Tian Z, Goodarzi M, Bandarra Filho EP, Arjomandi M (2019b) Thermal assessment of nano-particulate graphene-water/ethylene glycol (WEG 60: 40) nano-suspension in a compact heat exchanger. Energies 12(10):1929. https://doi.org/10.3390/en12101929

Shahsavar A, Khanmohammadi S, Karimipour A, Goodarzi M (2019) A novel comprehensive experimental study concerned synthesizes and prepare liquid paraffin-Fe3O4 mixture to develop models for both thermal conductivity and viscosity: a new approach of GMDH type of neural network. Int J Heat Mass Transf 131:432–441. https://doi.org/10.1016/j.ijheatmasstransfer.2018.11.069

Tiwari S, Gupta PK, Bagbi Y, Sarkar T, Solanki PR (2017) L-cysteine capped lanthanum hydroxide nanostructures for non-invasive detection of oral cancer biomarker. Biosens Bioelectron 89:1042–1052. https://doi.org/10.1016/j.bios.2016.10.020

Wang S, Chen ZG, Cole I, Li Q (2015) Structural evolution of graphene quantum dots during thermal decomposition of citric acid and the corresponding photoluminescence. Carbon 82:304–313. https://doi.org/10.1016/j.carbon.2014.10.075

Xia T, Liu C, Hu J, Guo C (2016) Article for chemical engineering journal improved performance of immobilized laccase on amine-functioned magnetic Fe_3O_4 nanoparticles modified with polyethylenimine. Chem Eng J. https://doi.org/10.1016/j.cej.2016.03.044

Yang HY, Li Y, Lee DS (2018) Multifunctional and stimuli-responsive magnetic nanoparticle-based delivery systems for biomedical applications. Adv Thear 1800011:1–17. https://doi.org/10.1002/adtp.201800011

Zhang R, Ding Z (2018) Recent advances in graphene quantum dots as bioimaging probes. J Anal Test 2(1):45–60. https://doi.org/10.1007/s41664-018-0047-7

Zhang R, Adsetts JR, Nie Y, Sun X, Ding Z (2018) Electrochemiluminescence of nitrogen-and sulfur-doped graphene quantum dots. Carbon 129:45–53

Zheng XT, Ananthanarayanan A, Luo KQ, Chen P (2015) Glowing graphene quantum dots and carbon dots: properties, syntheses, and biological applications. Small 11(14):1620–1636

Zhuo S, Shao M, Lee S-T (2012) Upconversion and downconversion fluorescent graphene quantum dots: ultrasonic preparation and photocatalysis. ACS Nano 6(2):1059–1064